Journal of Sound and Vibration (1999) **220**(5), 771–786
Article No. jsvi.1998.1999, available online at http://www.idealibrary.com.on IDEAL

NON-LINEAR DYNAMICS OF UNDERWATER ACOUSTICS

M. WIERCIGROCH

Department of Engineering, University of Aberdeen, King's College, Aberdeen AB24 3UE, U.K.

M. BADIEY

Ocean Acoustic Laboratory, Graduate College of Marine Studies, University of Delaware, Newark, DE 19716, *U.S.A.*

J. SIMMEN

Ocean Acoustics Program, Office of Naval Research, 800 *N. Quincy Street, Arlington, VA* 22217, *U.S.A.*

AND

A. H.-D. CHENG

Department of Civil and Environmental Engineering, University of Delaware, Newark, DE 19716, *U.S.A.*

(*Received* 21 *July* 1998)

The non-linear dynamic behavior of acoustic wave propagation in an underwater sound channel, described by the Munk's classical sound speed profile perturbed by a single-mode internal wave, is studied using a parabolic ray theory. The amplitude and wavelength of this single-mode wave are used as the branching parameters in bifurcation analysis. The phase plane trajectory of the ray-based system can be periodic, quasi-periodic, and unstable. The regions of instability, located numerically via the bifurcation diagrams, are examined through a sequence of phase diagrams and Poincaré maps. Charts showing the maximum uninterrupted propagation distance reveal instances of anomalous vertical scattering of sound energy. Floquet multipliers were used to investigate instability of periodic orbits.

1. INTRODUCTION

Interest has grown in recent years in the use of sound propagation as a tomographic means to study the ocean [1, 2]. The idea is quite simple: a sound source within the ocean generates pulses, and several receivers, horizontally and vertically displaced from the source, receive them. From the time delay of the received signals and a knowledge of ray paths, one inverts for the ocean's sound speed (or temperature) structure between the source and receivers. So far, arrival time has been the primary signal characteristic from which inversions have been

0022–460X/99/100771 + 16 $30.00/0

performed to reconstruct ocean structure. For long-range propagation (exceeding several hundred kilometers) it has been suggested [3] that ocean fluctuations (such as internal waves) destroy the utility of using arrival time as a characteristic upon which to build inversion schemes, and perhaps other signal properties (e.g., modal delays) may be more serving. Recent theoretical and experimental studies by Simmen *et al*. [4] have suggested that the breakdown in identifying isolated and resolved signal arrivals at long ranges is due to ray chaos induced by a range-dependent ocean structure. They also pointed out that this ray chaos can lead to a substantial increase in (micro) multipaths, which in turn, limits the spatial resolution of any tomographic inversion scheme based on the time-of-flight.

With the geometrical approximation (i.e., in the high frequency limit) the linear wave equation reduces to an eikonal and a transport equation. These equations are a system of non-linear ordinary differential equations, describing the behavior of signal arrival time and amplitude along ray trajectories. One coupled pair of these equations describes the ray trajectories, which forms a Hamiltonian system. This theoretical approach has been studied extensively for almost two decades by Zaslavsky's group, it is summarized in the recent review paper [5]. When the ocean medium through which the acoustic signal propagates contains a range-dependent structure, such as that due to internal waves and mesoscale fluctuations, then this Hamiltonian system is non-integrable and can exhibit notable sensitivity to initial conditions or environmental perturbations [6].

The present paper probes into the non-linear dynamic behavior of basic ray equations in the presence of a wave-like forcing assuming that a single-mode sound speed perturbation is superimposed onto a generic range-independent sound speed profile known as the Munk's canonical profile [7]. The goal is to investigate acoustic wave propagation using the ray equations for a simple ocean model, with the intent of later extending the methodology and understanding developed in this initial study to a more realistic ocean scenario. The analysis will be carried out using a non-linear dynamics approach (e.g., [8, 9]), in particular, stability analysis will be conducted by constructing bifurcation diagrams, Poincaré maps, and calculating Floquet multipliers. The internal wave parameters, namely the amplitude and wavelength, will be used as the branching parameters.

2. PARABOLIC RAY EQUATIONS

There is a number of computational means for the investigation of underwater sound wave propagation such as normal modes technique, spectral analysis, finite difference and finite elements methods and ray methods, to name a few [10], but the ray-based methods provide the best geometric insight into the nature of the long-distance wave propagation. Moreover, an outstanding agreement with the experimental results has been reported recently [4]. This will be discussed briefly later to support the choice of the ray method.

As prompted earlier, pulse travel time has been used as the principal signal characteristic to reconstruct ocean sound-speed tomography. However, for

propagations over long distances, it has been observed [11] that pulse timefront arrivals sometimes become so smeared that they cannot be used for the travel-time measurements. It is thought this is due to the internal waves acting on the sound-speed profile. A comparison of the actual and the simulated time front [4] is given in Figure 1. Figure 1(a) shows the reconstructed arrivals from the experimental result for a single pulse, while Figure 1(b) depicts the superposition of the simulated ray arrivals for three separate realizations of the internal-wave field. The distinguished, early-arriving timefront segments, the smearing of timefront in the rear of the pulse, and the envelope of the arriving rays compare well between the simulation and the actual case.

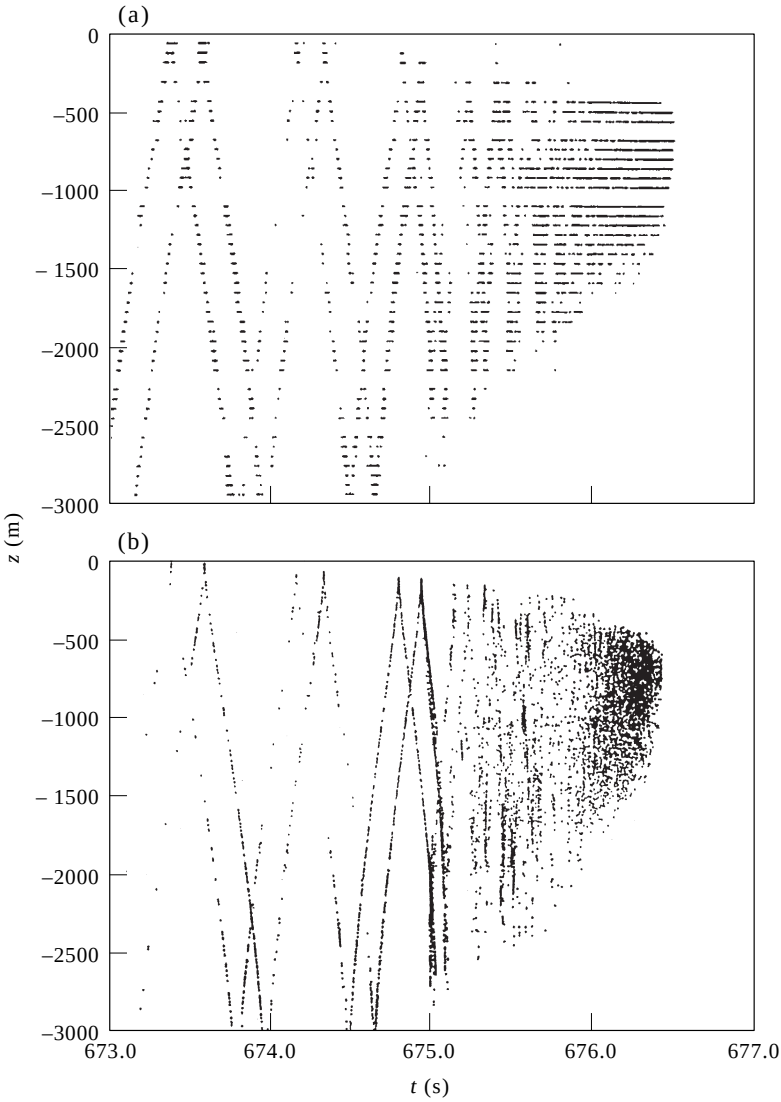

Figure 1. (a) Actual and (b) simulated timefront.

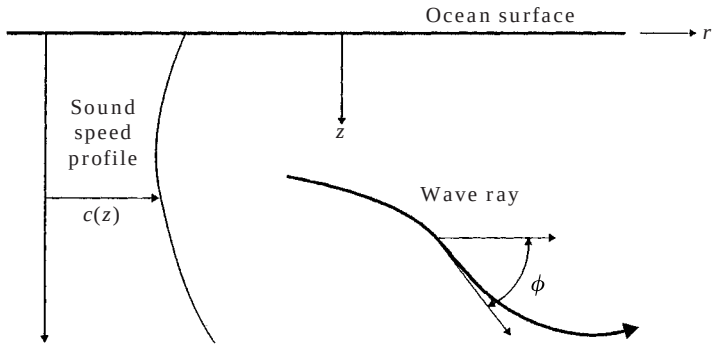

Figure 2. Definition sketch of acoustic ray.

As a result, the ray approach was chosen for the studies, where the eikonal equations can be elegantly expressed by the following pair of equations

$$\frac{\mathrm{d}z}{\mathrm{d}r} = \frac{\partial H}{\partial p}, \qquad \frac{\mathrm{d}p}{\mathrm{d}r} = -\frac{\partial H}{\partial z}, \tag{1, 2}$$

where H is a Hamiltonian of the following form

$$H(z, p) = \tfrac{1}{2}p^2 + V(z). \tag{3}$$

Here, z is the ray depth, r is the horizontal range, and $p = \tan\phi$ is the tangent of the ray angle ϕ with respect to the horizontal axis, which is schematically depicted in Figure 2. The potential energy function $V(z)$ depends on the average sound speed profile $c(z)$ in the ocean

$$V(z) = \frac{1}{2}\left[1 - \left(\frac{c_0}{c(z)}\right)^2\right], \tag{4}$$

where c_0 is a reference sound speed. The average sound speed profile $c(z)$ is calculated after Munk [7]

$$c(z) = c_a\left[1 + \varepsilon\left(\mathrm{e}^{-2(z - z_a)/B} + 2\frac{z - z_a}{B} - 1\right)\right]. \tag{5}$$

In this model of the sound speed profile, ε is a constant, z_a is the depth at the sound channel axis, c_a is the sound speed at the sound channel axis, and B is a scale depth.

So far, the propagated rays have been modelled as an energy conserving system, which in reality, is subjected to perturbations from the internal waves in mesoscale of the ocean. Such perturbations can be described in the first approximation by adding a range and depth dependent forcing function, $F(z, r)$, to the Hamiltonian (3) such that

$$H(z, p, r) = \tfrac{1}{2}p^2 + V(z) + F(z, r). \tag{6}$$

The effect on the ray dynamics of a single-mode internal wave, described by

$$F(z, r) = \sqrt{2}A\ \mathrm{e}^{-3z/2B} \sin \frac{2\pi r}{R} \tag{7}$$

will be investigated. Here A is the amplitude, and R is the wavelength of the internal wave. These two parameters, A and R, comprise a parameter vector for bifurcation analysis. Substituting equation (6) into equations (1) and (2), the resultant forms a non-autonomous set of non-linear ordinary differential equations

$$\frac{\mathrm{d}z}{\mathrm{d}r} = p, \tag{8}$$

$$\frac{\mathrm{d}p}{\mathrm{d}r} = -\frac{2}{B} c_0^2 c_a \varepsilon \frac{1 - \mathrm{e}^{-2(z - z_a)/B}}{c(z)^3} + \frac{3\sqrt{2}}{2B} A\ \mathrm{e}^{-3z/2B} \sin \frac{2\pi r}{R}. \tag{9}$$

These equations can be numerically integrated using a fourth order Runge–Kutta method, however, due to the fact that the system has a strong non-linearity, a careful monitoring of the integration step length is essential to maintain numerical accuracy and stability. In particular, for a certain length of integration step, an artificial parasite damping can occur and mislead the local stability picture.

3. BIFURCATION ANALYSIS

Recent developments in non-linear dynamics and chaos theory have brought a deeper insight into stability analysis via application of new techniques such as constructing Poincaré maps, bifurcation diagrams and Lyapunov exponents, to name a few, which are extensively discussed in references [8, 9, 12, 13]. One of the most useful techniques from an engineering applications point of view, is bifurcation analysis as by a means of a control parameter, one may investigate qualitative changes of the system dynamics. Construction of bifurcation diagrams differs for autonomous and non-autonomous systems [14]. For a non-autonomous system, a bifurcation diagram is constructed using Poincaré maps computed for different values of the branching parameter, which can be explained as follows. In the phase plane z–p, the mapping of $z_N \rightarrow z_{N+1}$ is taken at the z-axis ($p = 0$), where the flow crosses in the direction of $p^- \rightarrow p^+$ (see Figure 3). The points are recorded for each varying parameter and assembled as the bifurcation diagrams $z = f(A)$ or $z = f(R)$.

The parameter vector $\mathbf{p}$ used in these investigations is composed of only two elements, A and R. Using an analogy to a forced oscillator, parameters A and R correspond to the amplitude and the forcing frequency, respectively. The amplitude effect is examined in the first instance. Figures 4(a) and (b) show the bifurcation diagrams $z = f(A)$ for a fixed wavelength, $R = 1$ km, and the initial conditions $z = 1$ km and $\phi = \tan^{-1} p = 7{\cdot}5^\circ$. For the purpose of mathematical interest, an A range used is beyond the practical limit, say $A < 0{\cdot}01$. The bifurcation diagram depicted in Figure 4(a) suggests a periodic motion when plotted on the full scale of z. However, zooming in and plotting in a truncated

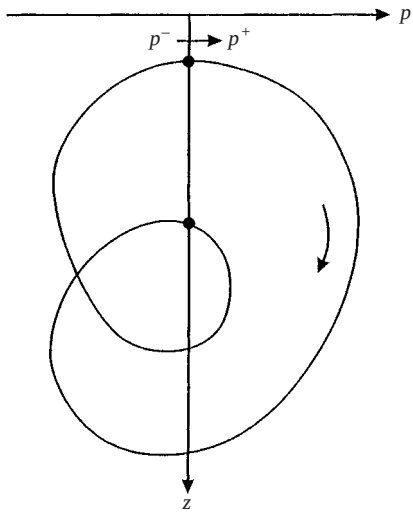

Figure 3. Construction of bifurcation diagram for autonomous system.

z scale as in Figure 4(b), a quasi-periodic motion is revealed. Unlike a dissipative system which requires excitation to maintain its motion, a Hamiltonian system preserves its energy. For a given set of the system parameters and initial conditions, the autonomous system has a unique natural frequency, ω_n. In addition, the system is forced with the internal wave, which in general has a different frequency, ω. Therefore, the resonance conditions may occur only for a finite set of frequency ratios. However, in the present case involving small forcing amplitude A, the so-called natural mode dominates, and this is evident from the observation of the phase diagrams. Figures 5(a) and (b) present the wave ray trajectories in the $z - \phi$ plane, computed for $A = 0{\cdot}03$ and two different propagation distances. Figure 5(a) plots the trajectory for the first 100 km of propagation, a distance of about two natural wavelengths. A perturbation of small amplitude and high frequency superimposed onto the natural mode is observed. The frequency (or wavelength, R) of the forcing, is incommensurate with the natural frequency, ω_n, hence, the trajectory does not close. A further continuation of the trajectory for a propagation distance up to 1000 km reveals a filled band

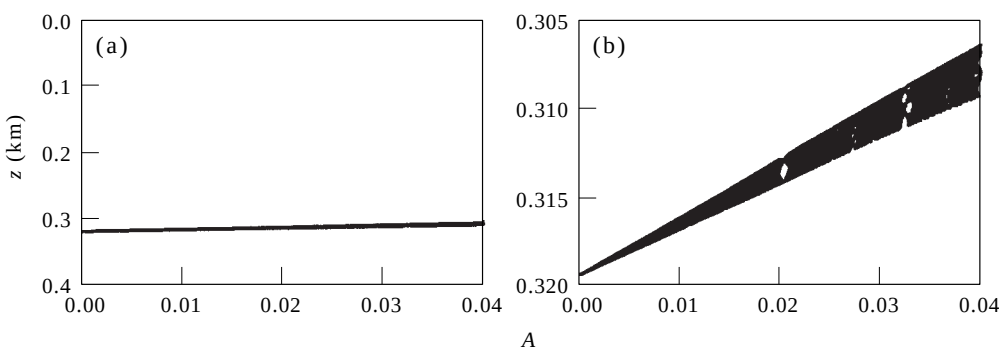

Figure 4. Bifurcation diagram $z = f(A)(R = 1$ km); (a) full scale, (b) zoom-in.

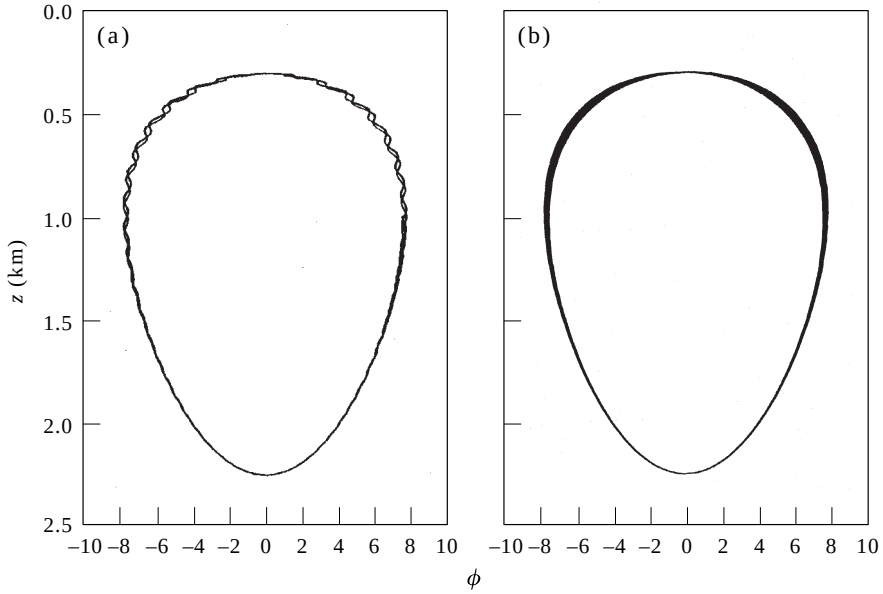

Figure 5. Phase planes ($A = 0{\cdot}03$, $R = 1$ km); (a) $r = 100$ km, (b) $r = 1000$ km.

(Figure 5(b)). These indications are consistent with the characteristics of a quasi-periodic motion. Quasi-periodicity does not break off or change to a different type of motion even for much larger amplitudes of forcing (see Figure 4(b)) and remain the only type of dynamic responses for $R = 1$. It may be concluded that for an internal wave perturbation of wavelength $R = 1$ km and a launch angle $7{\cdot}5^\circ$, wave rays remain trapped in the sound channel. This is valid for perturbation amplitude A even beyond the realistic range. The resultant modification of the ray trajectory involves only a small harmonic perturbation on top of the unperturbed natural mode.

The second branching parameter to be investigated is the wavelength, R, and the bifurcation diagrams $z = f(R)$ can provide even more significant insight into this dynamical system. The initial conditions and parameters used are $z(0) = 1$ km, $\phi(0) = 7{\cdot}5^\circ$, and $A = 0{\cdot}005$. The bifurcation diagram shown in Figure 6 was constructed for the internal wavelength R ranging from 0 to 40 km. It can be noted that the effect of the perturbation is small up to $R = 5$ km. After that, the system responses become irregular with increased amplitudes. To investigate this behaviour, a value of $R = 8{\cdot}1$ km was selected, i.e., the exact location of a spike in the bifurcation diagram. Figures 7(a) and (b) plot the phase planes for the propagation of 400 and 4000 km, respectively. As can be seen the trajectory loop does not close up even for 4000 km propagation (see Figure 7(b)). The response again reveals the characteristic of quasi-periodic motion and this is confirmed by a Poincaré map depicted in Figure 8. A cross-section of the attractor (the attracting set) is formed by six closed loops.

As R continues to increase, occasions in which the ray diverges and eventually intersects the ocean surface at $z = 0$ are observed. The first occurrence of this type is around $R = 12{\cdot}5$ km, and it becomes much more frequent for $R > 15$ km. It is

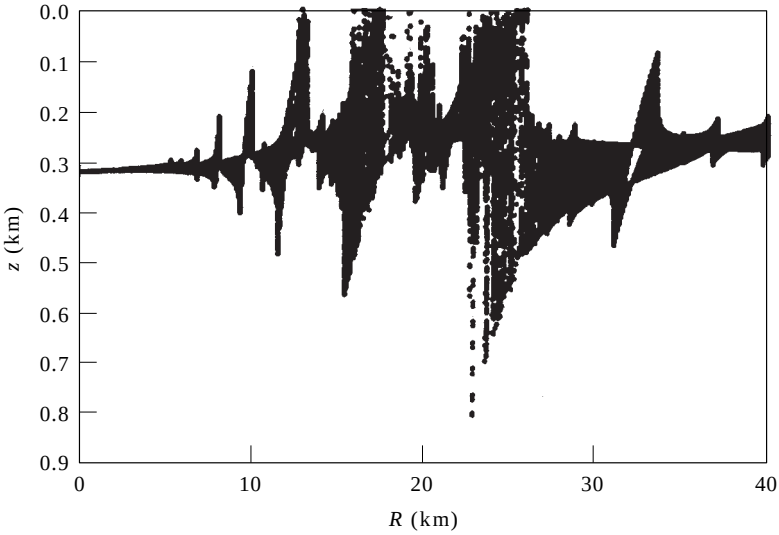

Figure 6. Bifurcation diagram $z = f(R)(A = 0{\cdot}005)$.

worth mentioning here, that surface reflection is not modelled in the present work to simplify the dynamics, however, this can be done by adopting the piecewise approach [15, 16]. This simplification, however, has a practical justification as the effectiveness of sound channelling diminished once a wave ray intersects the ocean surface losing a significant portion of its energy. The simulation hence terminates whenever that occurs. Two such ray incidences are shown in Figures 9(a) and (b) for $R = 17$ km and $R = 18$ km, respectively. For the first case (Figure 9(a)) a slow outward divergence of trajectory is observed, where the surface intersection takes

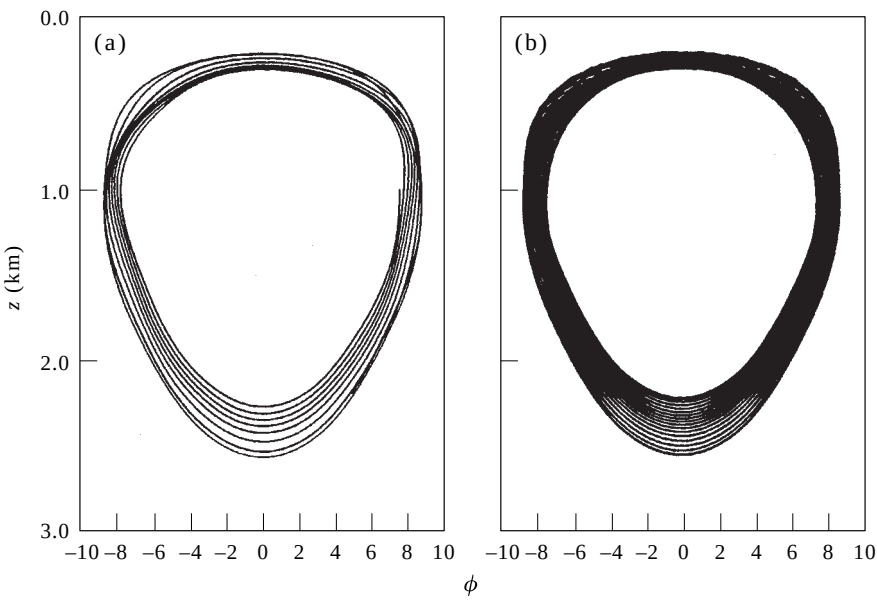

Figure 7. Phase planes ($A = 0{\cdot}005$, $R = 8{\cdot}1$ km); (a) $r = 400$ km, (b) $r = 4000$ km.

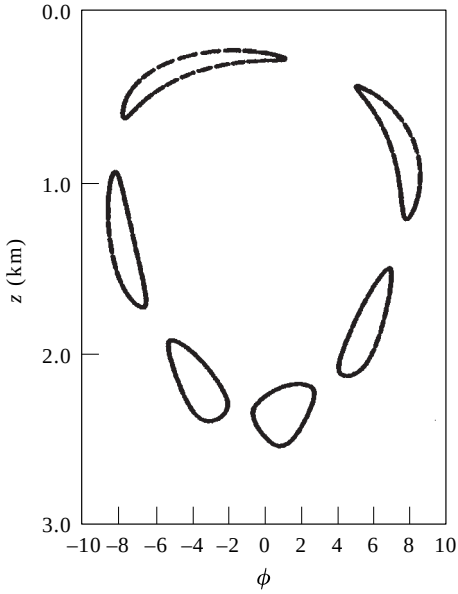

Figure 8. Poincaré map ($A = 0{\cdot}005$, $R = 8{\cdot}1$ km).

place around $r = 6000$ km. Although it has no longer physical meaning, the simulation can continue beyond the intersection by extending into the negative z range. In that case, it is revealed that the fate of the ray is exponential divergence toward infinity. This type of instability appears to be always heralded by a diffused Poincaré map, as shown in Figure 10. There are also cases in which the rate of

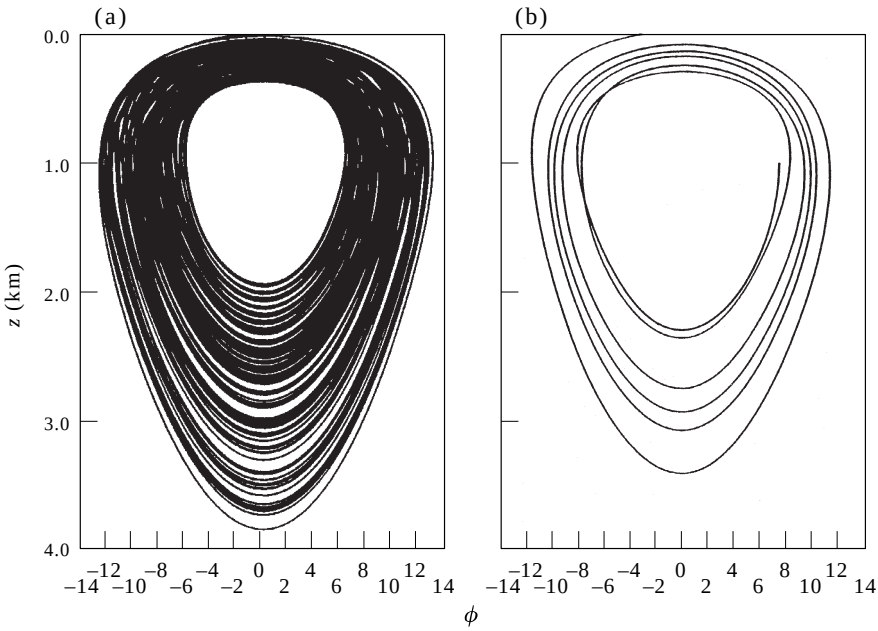

Figure 9. Phase planes ($A = 0{\cdot}005$); (a) $R = 17$ km, (b) $R = 18$ km.

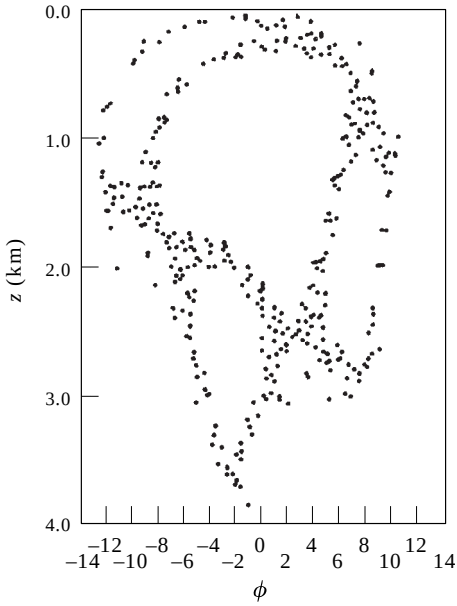

Figure 10. Poincaré map ($A = 0{\cdot}005$, $R = 17$ km).

divergence is so rapid that the system looses its stability after a very short propagation, so the ray intersects the ocean surface after only 300 km (see Figure 9(b)). For $R > 26$ km, the system becomes stable again, as can be seen from the Poincaré map shown in Figure 11, which was constructed for $R = 30$.

Establishing conditions for a long and undisturbed sound propagation is the primary interest of ocean acoustics. This can be supported by constructing

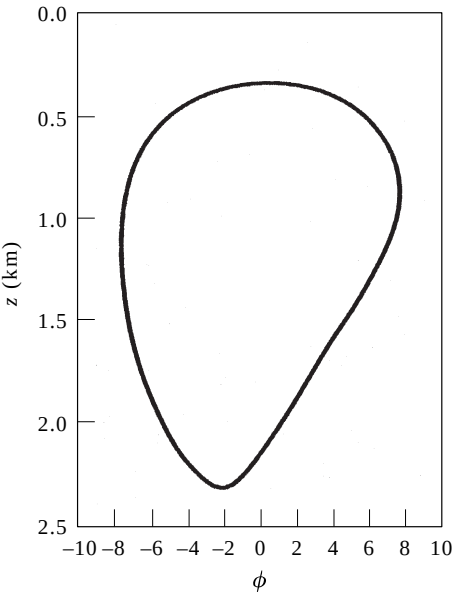

Figure 11. Poincaré map ($A = 0{\cdot}005$, R = 30 km).

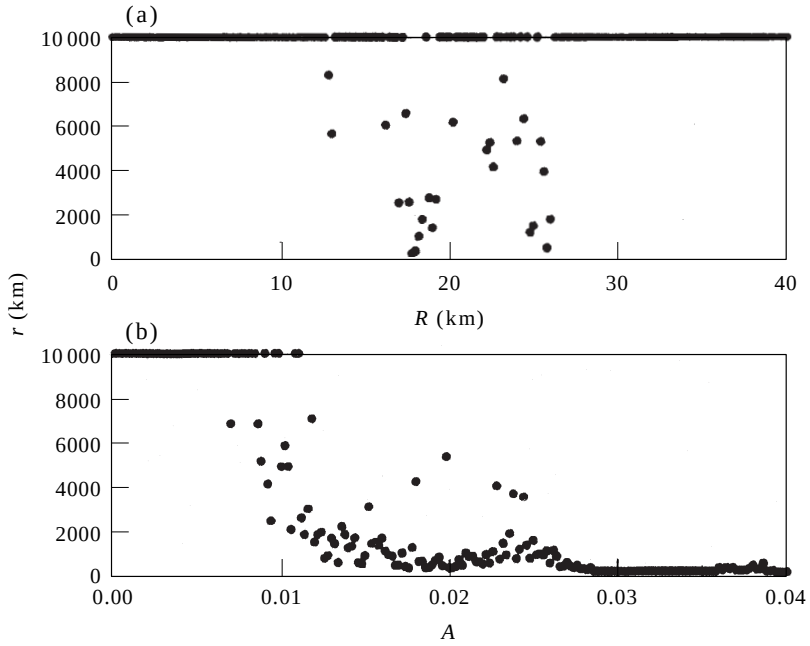

Figure 12. Maximum ray propagation range before intersection ocean surface; (a) $r = g(R)(A = 0{\cdot}005)$, (b) $r = g(A)(R = 10$ km).

bifurcation diagrams (e.g., Figure 6), which may be viewed as "design charts" showing the effectiveness of long-range propagation. For that purpose Figure 12 is constructed, where the maximum range r that a sound ray can travel before intersecting the ocean surface is calculated. The system parameters used are identical as for Figure 6. Since the simulation is terminated at $r = 10\,000$ km, a dot at that value implies infinite propagation range. By examining Figure 12(a) closer, it can be noted that the sound ray channelling is largely effective in this parameter range, except for a finite number of R values. Observations made in the real ocean suggest that some rays can scatter much more extensively in depth than predicted for an ocean without fine structure (e.g., internal waves), and in fact, the energy associated with these scattered rays has been detected at the ocean bottom, hundreds of meters deeper than expected [17]. It is suspected that ocean fluctuations (internal waves or internal tides) generate wavelengths that can scatter rays to the ocean bottom.

To investigate a poor propagation further shown in Figure 12(b), a bifurcation diagram $z = f(A)$ is constructed for R fixed at 10 km, and it is depicted in Figure 13. At small values of A the diagram suggests a stable unique solution. Zooming into that region shows four smeared lines, which practically speaking suggests a period-four motion. For such a behavior, it is worth noting that the excitation wavelength, $R = 10$ km, is roughly one-quarter of the wavelength of $L_o = 41{\cdot}6$ km calculated for the linear unforced system. This behavior continues until $A = 0{\cdot}0046$, where a sudden jump of amplitude is observed and the period-four co-exists with an irregular motion. Soon after that, at around $A = 0{\cdot}0070$, some wave rays start to intersect the ocean surface and the simulation is terminated at

that point. At even larger A values, some wave rays are highly unstable and the intersection takes place after only a few wavelengths. The maximum propagation distance is captured in Figure 12(b).

4. STABILITY OF PERIODIC ORBITS

As demonstrated in the preceding section, the system can exhibit stable and unstable (unbounded) trajectories. The stable ones take the form of periodic (for the unforced system or when the forcing frequency is locked) or quasi-periodic motion. Near subharmonic resonance, the trajectory might have a very long transient, or in other words, the system might exhibit asymptotic instability. This type of instability, which has not been reported in any earlier work for this ray system, will be investigated via Floquet theory.

The loss of stability of a periodic orbit can be examined by Floquet theory, and for this purpose equations (8) and (9) are rewritten into more general form

$$\mathbf{x}' = \mathbf{f}(\mathbf{x}, \mathbf{p}, r), \tag{10}$$

where $\mathbf{x} = [z, p]^T$ represents the two-dimensional phase space, $\mathbf{p} = [A, R]^T$ is the parameter space, and the prime marks the differentiation with respect to r. If the system has a periodic orbit Γ, its local stability in a small vicinity of the orbit can be assessed through linearised perturbed equations, which can be written as follows

$$\tilde{\mathbf{x}}' = \mathbf{J}(r)\tilde{\mathbf{x}}, \tag{11}$$

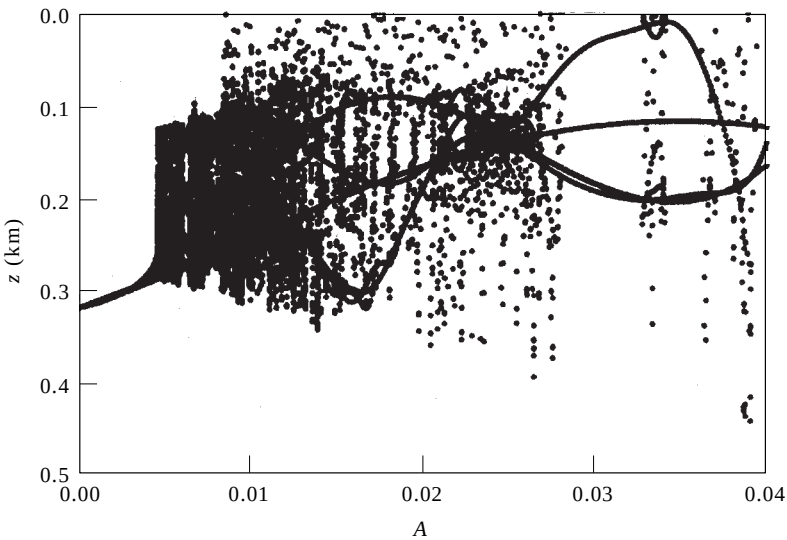

Figure 13. Bifurcation diagram $z = f(A)(R = 10\ \text{km})$.

where $\tilde{\mathbf{x}}$ is perturbation around the periodic trajectory, and $\mathbf{J}$ is the Jacobi matrix evaluated at $\mathbf{x}_e(r) \in \Gamma$,

$$\mathbf{J}(r) = \left.\frac{\partial \mathbf{f}}{\partial \mathbf{x}}\right|_{\mathbf{x}_e(r)}. \tag{12}$$

Due to the periodicity of the trajectory Γ, the Jacobian $\mathbf{J}(r)$ is a matrix with periodic elements. The solution of the perturbed linearised equation (11) can be written as a combination of independent linear solutions $\tilde{\mathbf{x}}_i(r)$,

$$\tilde{\mathbf{x}}(r) = \sum_{i=1}^{2} c_i \tilde{\mathbf{x}}_i(r). \tag{13}$$

This can be used to form a fundamental solution system, which may be expressed in a matrix form as follows

$$\tilde{\mathbf{x}}(r) = \mathbf{\Phi}(r)\mathbf{C}, \tag{14}$$

where $\mathbf{\Phi}(r)$ is an $n \times n$ $(n = 2)$ matrix composed of the n linearly independent fundamental solution vectors, and $\mathbf{C}$ is an $n \times n$ matrix known as the monodromy matrix. For the system of fundamental solutions, the initial conditions have been chosen as a unit hypersphere, i.e.,

$$\mathbf{\Phi}(0) = \mathbf{I}, \tag{15}$$

where $\mathbf{I}$ is the identity matrix. The monodromy matrix plays a crucial role as its eigenvalues λ, so-called Floquet multipliers, provide the necessary information concerning the stability of the periodic solution $\mathbf{x}_e(r)$. Substituting the fundamental solution into equation (14), with the initial distance $r = 0$, and assuming periodicity of wavelength, L, it can be shown

$$\mathbf{\Phi}(L) = \mathbf{C}, \tag{16}$$

which can be utilized to calculate the monodromy matrix by integration of the system (11) applying the initial conditions as in equation (15).

To construct the monodromy matrix $\mathbf{C}$, the perturbed system (11) with the two sets of initial conditions, $(\tilde{z}_0, \tilde{p}_0) = (1, 0)$ and $(0, 1)$, as defined in equation (15), is numerically integrated side-by-side with the non-autonomous system, (8) and (9), with its original initial conditions. The original system is used in the capacity of numerically identifying the period (wavelength) L, thus terminating the integration. The final solution vectors $\tilde{\mathbf{x}}(L)$ are assembled to form the monodromy matrix. Their eigenvalues λ are the Floquet multipliers. An absolute value $|\lambda| > 1$ for any of the eigenvalues indicates an unstable orbit.

It should be mentioned here the above outlined procedure can be used in a rigorous manner only for a pure periodic orbit. As observed in the preceding section, some of the system responses are quasi-periodic, where their orbits never close up. Some difficulty is expected in the interpretation of maximum Floquet multipliers for such cases. Nevertheless, since the perturbation introduced by the forcing is small, it is possible to identify an approximate period when the trajectory

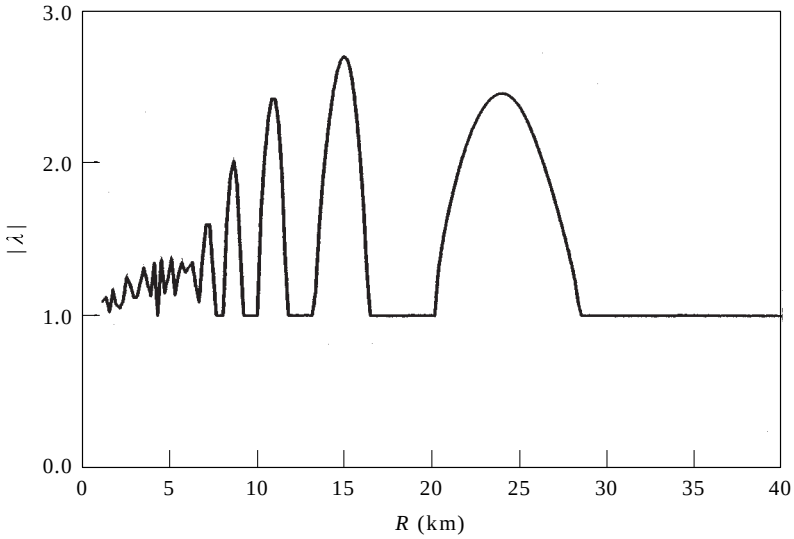

Figure 14. Floquet multiplier diagram ($A = 0{\cdot}005$).

returns to a close vicinity of, but not the same, starting position. With such a pragmatic approach, the calculated maximum Floquet multiplier will be a good indicator of the system stability. The computation of the Floquet multipliers is achieved by integration of merely one cycle. However, due to the quasi-periodicity complication, it is suspected that the analysis based only on the Floquet multipliers may lead to inaccurate results for the cases when the system is stable, especially in the range of small internal wavelength, R. This is illustrated by an example below.

The Floquet analysis is applied to the same case, as illustrated in Figure 6. The result of the analysis is shown as $|\lambda|$ versus R in Figure 14. At larger values of R the following observation was made. In the predicted stable region, two complex conjugate eigenvalues of absolute values exactly equal to 1 were found. Otherwise, two real eigenvalues exist, where the larger is always greater than 1 and this marks the unstable region. Based on this criterion, it was predicted that the unstable region should lie between 13 km $< R <$ 16 km, and 20 km $< R <$ 28 km. A close look at Figure 6 does confirm bursts of instabilities around these regions. For $R <$ 10 km, the Floquet multiplier becomes noisy, which indicates instability, however, this is not born out by a long term simulation, as in Figure 6.

Considering quasi-periodicity as another form of stability, it is believed an appropriate procedure can be devised for calculating Floquet multipliers. One possibility is to extend the traditional definition of Floquet multiplier to consider its transient values at multiple cycles of quasi-periodic trajectory. A preliminary analysis and numerical experiment shows that the Floquet multiplier averaged over the quasi-periodic cycles can cure much of this anomaly. As there is no precedence of such an analysis, a more rigorous and complete study is needed before jumping to the conclusion. However, this part is left for a future investigation.

5. CONCLUDING REMARKS

The dynamics of sound rays lend insight into the behavior of acoustic propagation in the ocean wave guide. With the forcing from an internal wave, is superimposed on the Munk's canonical sound speed profile, an otherwise simple harmonic ray trajectory can become a complex one. Utilizing various non-linear dynamics tools, such as the construction of bifurcation diagrams, phase planes and Poincaré maps, and the computing of Floquet multipliers, the dynamics of the ray system can be better understood.

To achieve an early detection of instability of these nearly periodic (quasi-periodic) motions, Floquet analysis is applied. A straightforward application, however, leads to inconclusive results. At larger forcing wavelength, the Floquet multiplier seems to be a good indicator of instability. At small forcing wavelength, the interpretation is not straightforward. Although some clues appear obtainable from the study of quasi-periodic motions via Floquet theory, which suggests an extension of the definition of Floquet multiplier by averaging it in time, this area requires further research.

Bifurcation diagrams (such as Figures 6 and 13) demonstrate the various regimes of sound ray behavior. Charts such as Figure 12 showing the maximum propagation distance, also display additional useful information, i.e., the fractal appearance in some regions might explain the observed sporadic ray scattering into greater depths under otherwise normal propagation conditions. Generally speaking, these and other innovative diagrams may be used as "design charts" for predicting the behavior of ocean sound propagation under various environmental and operational conditions or for non-linear dynamic control purposes (e.g., [18, 19]).

A later refinement might include multi-mode internal wave perturbations and ray reflection from a rough ocean surface and bottom but is not considered presently so as not to confuse the fundamental non-linear dynamic issues discussed herein. For long-range propagation, ignoring rays that reflect from the ocean surface or bottom is justified anyway, since these rays are severely attenuated over long ranges.

ACKNOWLEDGMENT

The support provided to the first author by the U.S. Government in the form of a Senior Fulbright Fellowship is deeply appreciated. The hospitality of the Civil and Environmental Engineering Department, and the College of Marine Studies, at the University of Delaware is also gratefully acknowledged. JS and MB would like to acknowledge the support of the Scientific Officer Research Program (SORP) at ONR.

REFERENCES

1. W. H. Munk and C. Wunsch 1979 *Deep Sea Research* **26A**, 123–161. Ocean acoustic tomography: a scheme for large-scale monitoring.

2. J. Spiesberger and K. Metzger 1991 *Journal of Geophysical Research* **96**, 4869–4889. Basin-scale tomography: a new tool for studying weather and climate.
3. J. Colosi, S. Flatte and C. Bracher 1994 *Journal of the Acoustical Society of America* **96**, 452–468. Internal-wave effects on 1000-km oceanic acoustic pulse propagation: simulation and comparison with experiment.
4. J. Simmen, S. M. Flatte and G.-Y. Wang 1997 *Journal of the Acoustical Society of America* **102**, 239–255. Wavefront folding, chaos, and diffraction for sound propagation through ocean internal waves.
5. G. M. Zaslavsky, M. Edelman and B. A. Niyazov 1997 *Chaos* **7**, 151–181. Self similarity, renormalization and phase nonuniformity of Hamiltonian chaotic dynamics.
6. G. M. Zaslavsky and S. S. Abdullaev 1997 *Chaos* **7**, 182–186. Chaotic transmission of waves and "cooling" of signals.
7. W. H. Munk 1974 *Journal of the Acoustical Society of America* **55**, 220–226. Sound channel in an exponentially stratified ocean with application to SOFAR.
8. J. M. T. Thompson and H. B. Stewart 1987 *Nonlinear Dynamics and Chaos*. New York: Wiley.
9. W. Szemilinska-Stupnicka 1990 *The Behaviour of Nonlinear Vibrating Systems*. Niholf.
10. F. B. Jensen, W. A. Kuperman, M. B. Porter and H. Schmidt 1994 *Computational Ocean Acoustics*. AIP Press.
11. B. D. Cournelle, P. F. Worcester, J. A. Hildebrand, W. S. Hodgkiss Jr., T. F. Duda, J. Boyd, B. M. Howe, J. A. Mercer and R. C. Spindel 1993 *Journal of Geophysical Research* **98**, 16365–77. Ocean acoustic tomography at 1000-km range using wavefronts measured with a large-aperture vertical array.
12. V. I. Arnold 1988 *Geometry Methods in the Theory of Ordinary Differential Equations*. Berlin: Springer; 2nd edition.
13. S. Wiggins 1990 *Introduction to Applied Nonlinear Dynamical Systems and Chaos*. Berlin: Springer.
14. T. S. Parker and L. O. Chua 1989 *Practical Numerical Algorithms for Chaotic Systems*. Berlin: Springer.
15. S. Natsiavas 1990 *Journal of Sound and Vibration* **141**, 97–102. Stability and bifurcation analysis for oscillators with motion limiting constrains.
16. S. Natsiavas 1993 *Journal of Sound and Vibration* **165**, 439–453. Dynamics of multi-degree-of-freedom oscillators with colliding components.
17. H. G. Schneider 1994 in *Theoretical and Computational Acoustics*: *International Conference on*, *Vol*. 2, *Environmental Acoustics* (eds. D. Lee and M. H. Schultz), Mystic, CN. World Scientific Publ. Singapore: Stochastic ray tracing.
18. E. Ott, C. Grebogi and J. A. Yorke *Physical Review Letters* **64**, 1196–1199. Controlling chaos.
19. T. Kapitaniak *Journal of Sound and Vibration* **163**, 182–187. Analytical methods of controlling chaos in Duffing's oscillator.